Research Article

Nano Research
2022, 15(2): 1246–1253

ISSN 1998-0124 CN 11-5974/O4
https://doi.org/10.1007/s12274-021-3632-4

Engineering cobalt sulfide/oxide heterostructure with atomically mixed interfaces for synergistic electrocatalytic water splitting

Xiaoyang Wang[1,§], Yu He[1,§], Xiaopeng Han[1] (✉), Jun Zhao[1], Lanlan Li[2], Jinfeng Zhang[1], Cheng Zhong[1], Yida Deng[1] (✉), and Wenbin Hu[1]

[1] *School of Materials Science and Engineering, Tianjin Key Laboratory of Composite and Functional Materials, Key Laboratory of Advanced Ceramics and Machining Technology of Ministry of Education, Tianjin University, Tianjin 300072, China*
[2] *School of Materials Science and Engineering, Hebei University of Technology, Tianjin 300130, China*
[§] *Xiaoyang Wang and Yu He contributed equally to this work.*

Received: 30 March 2021 / **Revised:** 27 May 2021 / **Accepted:** 30 May 2021

ABSTRACT

It remains challenging to develop economical and bifunctional electrocatalysts toward oxygen/hydrogen evolution reactions (OER/HER). Herein, we construct Co_9S_8 nanoflakes decorated Co_3O_4 nanoarrays with enriched heterogeneous interface zones on Ni foam (Co_9S_8@Co_3O_4/NF) via a novel step-wise approach. The Co_9S_8@Co_3O_4/NF hybrid manifests excellent performance with low overpotentials of 130 mV for HER (10 mA·cm^{-2}) and 331 mV for OER (100 mA·cm^{-2}), delivering a small voltage of 1.52 V for water splitting at 10 mA·cm^{-2} as well as outstanding catalytic durability, which surpasses precious metals and previously reported earth-abundant nanocatalysts. Further experimental and theoretical investigations demonstrate that the excellent performance is attributed to the followings: (i) Highly conductive Ni facilitates the efficient charge transfer; (ii) porous core-shell nanoarchitecture benefits the infiltration and transportation of gases/ions; (iii) heterogeneous interface zones synergistically lower the chemisorption energy of hydrogen/oxygen intermediates. This work will shed light on the controllable synthesis and engineering of heterostructure nanomaterials for clean energy storage and conversion technologies.

KEYWORDS

nanocomposite, heterointerface, electrocatalysis, oxygen evolution reaction, hydrogen evolution reaction

1 Introduction

Energy crisis and environmental pollution problems motivate people to seek new alternatives to traditional fossil fuels [1–3]. Concerned about the energy conversion efficiency and environmental friendliness of new energy devices, hydrogen energy has been widely regarded as one of the most appealing candidates [4–6]. Among various hydrogen production methods, water electrolysis is a promising and sustainable approach due to its simplicity and efficiency [7–10]. It is well known that the process of electrically promoted water-splitting includes two parts: oxygen evolution reaction (OER) on the cathode and hydrogen evolution reaction (HER) on the anode. However, because of the intrinsically sluggish catalytic kinetics of the two reactions, a much higher overpotential than the theoretical value is needed to be applied to the electrochemical system [11–13]. It is urgently required to develop a highly efficient and stable electrochemical catalyst to reduce the thermodynamic overpotential and thus promote energy conversion [9]. At present, noble metal-based materials (typically RuO_2 and IrO_2) present good OER performance [14], and Pt-based metals are highly active for catalyzing HER [15, 16], respectively. However, constrained by their scarcities, exorbitant price, poor stability, and unsatisfied bifunctional properties, they cannot be utilized at a large scale for commercial applications.

In the past decades, transition metals (e.g., Co, Fe, Ni, Mo) and their compounds have been extensively exploited for water electrolysis owing to their low cost, elemental abundance and environmental friendliness [17–21]. Among them, transition metal oxides (TMOs, e.g., Co-based oxides) are particularly attractive because of their flexible crystal structures, rich redox sites and strong corrosion resistance in an alkaline environment [22–26]. Unfortunately, one major issue for TMO materials is the inherent poor conductivity, which is traditionally overcome by compositing with carbon nanostructures [27, 28]. Moreover, although the TMO-based catalysts exhibit remarkable OER performance, their HER activities lie far behind the practical requirements, bringing challenges to constructing the bifunctional electrode. It is imperative to simultaneously reduce the formation energy of hydrogen and oxygen intermediates to accelerate the water-splitting process [29]. Recently, benefiting from the intrinsically enhanced electrical transfer capability and novel surface configuration, sulfides have been proved to possess highly efficient HER activities, especially the cobalt sulfides [30–33]. Furthermore, it has been recognized that fabricating transition metal-based heterostructures is favorable for catalytic performance enhancement due to increased active sites, modified electronic structures, enhanced electrical conductivity and optimized chemisorption strength for reactants [34–36]. Therefore, in the context of developing cost-effective electrode materials, it deserves particular interest to explore bifunctional and competitive electrocatalyst for both

Address correspondence to Xiaopeng Han, xphan@tju.edu.cn; Yida Deng, yida.deng@tju.edu.cn

HER and OER based on transition metal oxide and sulfide hybrid components. This implies the significance of heterojunctions involving both HER and OER active species, which can effectively tune the atomic and electronic configurations for synergistic chemisorption of H* and OH^- reactants on the surface [37], greatly accelerating the water decomposition kinetics.

Meanwhile, catalyst architecture should be rationally designed, whereas the regulated heterointerfaces must be fully exposed and benefit the transmission of mass/charge [38, 39]. Under this circumstance, one-dimensional (1D) nanoarray structures were vertically grown on conductive substrates, representing promising candidates owing to the large surface area, efficient charge transport and gas bubble release kinetics [31, 40]. Moreover, the *in-situ* fabricated integrated electrode can eliminate the use of polymer binder, decrease the series resistance and increase the adhesion of active phases on current-collecting supports, contributing to enhanced activity and durability of the resultant electrode [41, 42]. Therefore, engineering the oxide/sulfide heterointerface composites with self-supported nanoarray structures shows great potential to achieve high-efficiency overall water splitting.

Herein, we successfully synthesized a hierarchical integrated electrode with Co_9S_8 nanoflakes wrapped on Co_3O_4 nanoneedles heterostructure arrays in-situ grown on Ni foam (Co_9S_8@Co_3O_4/NF) through a controlled step-wise strategy, which displays much-enhanced performance towards overall water splitting in alkaline medium. The as-prepared core–shell Co_9S_8@Co_3O_4/NF nanocomposite enhances the contact with the electrolyte and introduces abundant chemically coupled heterogeneous interface zones between Co_9S_8 and Co_3O_4, thereby providing plenty of active sites with high activity for hydrogen and oxygen electrocatalysis. Additionally, the binder-free nanoarray *in-situ* grown on nickel foam guarantees faster electron transfer rates and long-term catalytic stability. Consequently, Co_9S_8@Co_3O_4/NF heterostructure manifests superior catalytic performance with low overpotentials of 130 mV at 10 mA·cm^{-2} for HER and 331 mV at 100 mA·cm^{-2} for OER in 1.0 M KOH. Furthermore, the Co_9S_8@Co_3O_4/NF electrode delivers a low cell voltage of 1.52 V at 10 mA·cm^{-2} for overall water splitting, which even surpasses that of the precious metal catalyst (Pt/C + RuO_2, 1.56 V) and most active earth-abundant materials reported previously. Otherwise, the almost negligible activity degradation after a 50-h period at a water-splitting current density of 10 mA·cm^{-2} suggests excellent long-term catalytic durability. Further experimental and theoretical investigations demonstrate that the unique hierarchical structure of conductive Ni foam can provide sufficient contact area and efficient charge transfer. Meanwhile, the *in-situ* generated heterogeneous interface zone between Co_9S_8 and Co_3O_4 can afford a large number of highly active sites that are favorable for chemisorption of hydrogen and oxygen intermediates, collectively contributing to the outstanding performance for overall water splitting.

2 Experimental

2.1 Material preparations

Preparation of $Co(CO_3)_{0.5}(OH)_{0.11}\cdot H_2O$/NF precursor: First, 0.6 g (1 mmol) urea, 0.148 g (4 mmol) NH_4F and 0.58 g (2 mmol) $Co(NO_3)_2\cdot 6H_2O$ were added in 40 mL deionized (DI) water. Then the reaction mixture was transferred into a 50 mL Teflon-lined stainless-steel autoclave along with a pretreated Ni foam with the size of 2 cm × 3 cm and aged at 90 °C for 10 h. As the reactor was cooled down to room temperature, the $Co(CO_3)_{0.5}(OH)_{0.11}\cdot H_2O$/NF was obtained by rinsing with DI water and ethanol several times and finally dried in an electric oven.

Preparation of Co_3O_4/NF: Above $Co(CO_3)_{0.5}(OH)_{0.11}\cdot H_2O$/NF was annealed in a muffle furnace at 300 °C for 2 h, totally converted into Co_3O_4/NF. Then the Co_3O_4/NF was cooled with the furnace to room temperature, washed with DI water three times and dried at 60 °C.

Preparation of Co_9S_8@Co_3O_4/NF: A series of different quantities of $Na_2S\cdot 9H_2O$ (0.2, 0.4, 0.6 and 0.8 g) were completely dissolved in 40 mL DI water and reacted with the Co_3O_4/NF in 50 mL Teflon-lined stainless steel autoclaves at 120 °C for 10 h. Finally, the samples with the average loading capacity of 2 mg·cm^{-2} were obtained.

Preparation of Co_9S_8/NF: $Na_2S\cdot 9H_2O$ (1.6 g) was added in 40 mL DI water, then the solution and a Co_3O_4/NF were transferred into a 50 mL reactor and reacted at 120 °C for 14 h. After cooled to room temperature, the obtained Co_9S_8/NF was washed with DI water three times and dried at 60 °C.

2.2 Electrochemical measurements

Electrochemical catalytic activity (HER and OER) measurements were conducted on a CHI760e electrochemical workstation. A standard three-electrode system was adopted, including a 1 cm × 1 cm platinum plate as the counter electrode in OER and a carbon rod as the counter electrode in HER, a mercuric oxide electrode (MOE) as the reference electrode, 1 cm × 1 cm prepared sample as the working electrode, and 1.0 M KOH solution as electrolyte. The contrast electrode samples of Pt/C/NF and RuO_2/NF were made by the following method: Firstly, 3 mg Pt/C (20 wt.%) powder or RuO_2 powder was dispersed in 970 μL isopropyl alcohol; then 30 μL 5 wt.% Nafion was added into the solution as the binder and the mixture was sonicated for 30 min to obtain the uniform ink; finally, 670 μL catalyst ink was dropped on a 1 cm × 1 cm Ni foam (with a mass loading of 2 mg·cm^{-2}). The potential was adjusted against reversible hydrogen electrode (RHE) by the equation: $E_{RHE} = E_{MOE} + 0.098\ V + 0.059 \times pH$. The cyclic voltammetry (CV) ranges from 0 V to 0.9 V vs. MOE for OER and from −0.7 V to −1.5 V vs. MOE for HER at 50 mV·s^{-1}. The polarization curves were measured by the linear sweep voltammetry (LSV) method at a scan rate of 5 mV·s^{-1}. The geometric double-layer capacitance (C_{dl}) was derived from CV curves at 5, 10, 25, 50, and 100 mV·s^{-1} from −0.05 to 0.05 V vs. MOE. Electrochemical impedance spectroscopy (EIS) measurements were carried out at 0.7 V vs. MOE for OER and −1.35 V vs. MOE for HER from 10^5 to 0.1 Hz with an AC potential amplitude of 5 mV. Galvanostatic measurements were applied on the OER and HER over a period of 180,000 s at 10 and −10 mA·cm^{-2}, respectively. Moreover, the catalytic performance of the samples for overall water splitting was measured in a two-electrode system. Two identical samples were used as both anode and cathode, while to the contrast electrode samples, the RuO_2/NF was used for OER and the Pt/NF was used for HER. The long-term stability was measured by chronoamperometry at a constant current density of 10 mA·cm^{-2}. The Faradaic efficiency (FE) was obtained by dividing the theoretical gas volume value by the actual gas volume value, and the gas volume was measured by the drainage method.

2.3 Material characterizations

The crystal structure of the samples was characterized by X-ray diffraction (XRD) (Rigaku D/Max 2500 V/PC). The morphology of the samples was characterized by a scanning electron microscope (SEM, Hitachi S-4800) equipped with an energy-dispersive spectrometer (EDAX Genesis XM2). A transmission electron microscope (TEM, JEOL JEM-2100F) was also used

to observe the structure. The chemical valence state was detected by X-ray photoelectron spectroscopy (XPS, Escalab 250, Thermo Scientific, USA). The physical surface area was measured by Brunauer–Emmett–Teller (BET) using an AutosorbiQ instrument (Quantachrome, US) at liquid-N_2 temperature.

2.4 Density functional theory (DFT) computational methods and details

All calculations were performed using the plane-wave pseudopotential method in the framework of DFT [43]. The ion core and valence electron interaction were described by Vanderbilt-type ultrasoft pseudopotential [44]. The exchange-correlation interactions were treated by the generalized gradient approximation (PBE/GGA) scheme [45]. The kinetic energy cutoff was set to 350 eV. The convergence thresholds between optimization cycles for energy change and maximum force were set as 10^{-5} eV·atom^{-1} and 0.03 eV·Å^{-1}, respectively. Surfaces of Co_3O_4 and Co_9S_8 were constructed using slab models with a vacuum thickness of 12 Å to avoid the interaction between periodic images. For Co_3O_4-Co_9S_8 heterostructures, the S-doped Co_3O_4 and O-doped Co_9S_8 surfaces were constructed to simulate the heterogeneous interfaces.

The free energies of adsorbed species (H and OH) are defined as $\Delta G_{(H/OH)} = \Delta E_{(H/OH)} + \Delta E_{zpe} - T\Delta S$, where $\Delta E_{(H/OH)}$ is the adsorption energy of adsorbed species from DFT calculation. ΔE_{zpe} and ΔS are the difference in zero-point energies and entropy during the reaction, respectively. Free energies calculation details can refer to the previous reports [46–48].

3 Results and discussion

The synthetic processes for Co_9S_8@Co_3O_4/NF nanocomposite are schematically illustrated in Fig. 1. The porous hybrid nanoarrays of Co_9S_8 nanoflakes wrapped Co_3O_4 nanoneedle on Ni foam were obtained by a step-wise strategy, including hydrothermal, oxidation and ion exchange sulfurization. Firstly, the $Co(CO_3)_{0.5}(OH)_{0.11}·H_2O$ nanoneedles were fabricated on Ni foam by hydrothermal method and then were annealed to form Co_3O_4/NF through removing H_2O and CO_2. Subsequently, in the process of hydrothermal sulfuration, a high concentration of sulfur is adsorbed on the surface of cobalt oxide firstly. Then, the sulfur diffuses inward to replace part of oxygen atoms, causing a lattice distortion; at the same time, cobalt diffuses outward driven by the concentration difference and combines with sulfur to form cobalt sulfide, which is assembled on the Co_3O_4 matrix to obtain the final core–shell Co_9S_8@Co_3O_4/NF

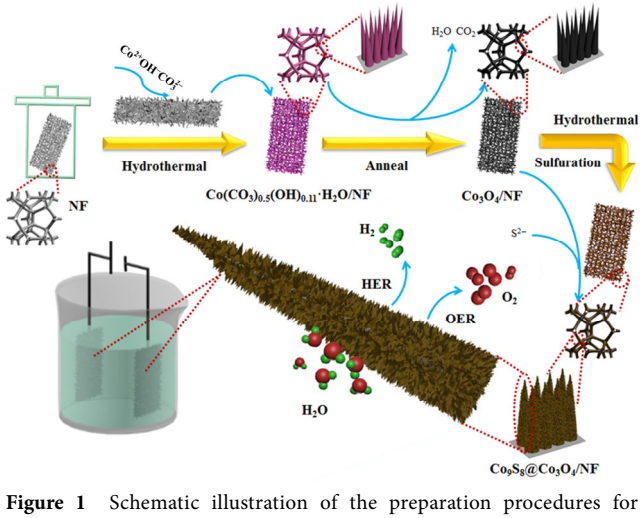

Figure 1 Schematic illustration of the preparation procedures for Co_9S_8@Co_3O_4/NF heterostructure hybrid electrode.

[49–52]. Figure S1 in the Electronic Supplementary Material (ESM) exhibits the visible change of the fabricated integrated electrode after every synthesis step. A large number of nanoflakes not only provide more nanointerface structures but also increase the specific surface area. An excessive concentration of Na_2S during the ion exchange process leads to the generation of pure Co_9S_8 on the Ni foam support (see details in the experimental section).

The phase structure of the prepared samples was characterized as shown in Fig. 2(a). In addition to the metallic nickel peaks at 44.5°, 51.8° and 76.4°, other diffraction peaks are distinct and well-indexed to the cubic Co_3O_4 (JCPDS 43-1003) or the cubic Co_9S_8 (JCPDS 02-1459), confirming the mixed-phase structure in Co_9S_8@Co_3O_4/NF. No peak of $Co(CO_3)_{0.5}(OH)_{0.11}·H_2O$ appears in Co_3O_4/NF, and no peak from cobalt oxide appears in Co_9S_8/NF, proving that all catalysts have been fully converted into target samples.

Figure S2 in the ESM presents the phase and morphology of $Co(CO_3)_{0.5}(OH)_{0.11}·H_2O$/NF precursor, which exhibits a nanoneedle array structure with a smooth surface. The Co_3O_4/NF maintains the morphology from the $Co(CO_3)_{0.5}(OH)_{0.11}·H_2O$/NF (Fig. S3(a) in the ESM), indicating that the heat treatment with the escaping of CO_2 and H_2O cannot destroy the whole architecture. As for the Co_9S_8@Co_3O_4/NF (Fig. S3(b) in the ESM), the nanoneedle arrays are corroded by S^{2-} and a large number of nanoflakes are *in situ* formed on the surface of the original nanostructure. Due to the mild sulfurization process by anion exchange growth, the needle-like nanoarrays structure has not been destroyed. Thus, the novel hierarchical nanoarchitecture possesses an extremely high specific surface area that can provide abundant electrochemical active sites. From the SEM image of Co_9S_8/NF (when excessive Na_2S is used, Fig. S3(c) in the ESM), the Co_3O_4 nanoneedle arrays have completely transformed into Co_9S_8 nanoflakes covering the whole surface.

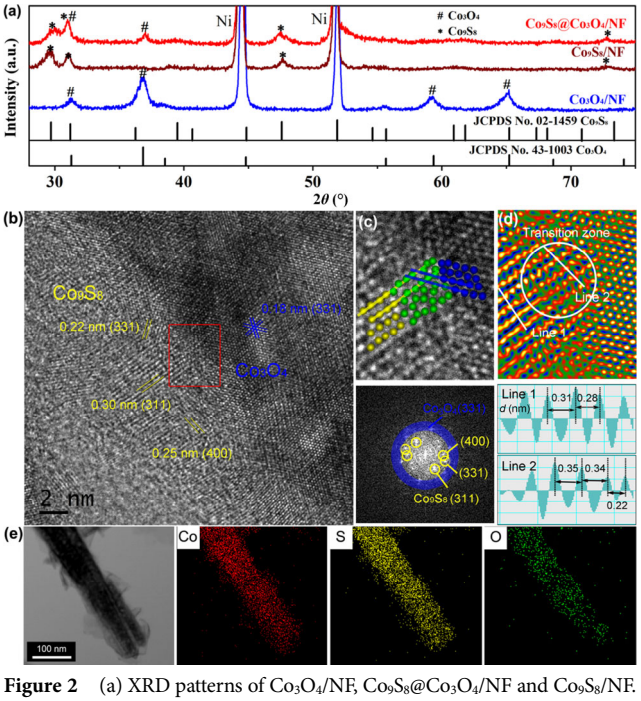

Figure 2 (a) XRD patterns of Co_3O_4/NF, Co_9S_8@Co_3O_4/NF and Co_9S_8/NF. (b) High-resolution TEM image of Co_9S_8@Co_3O_4/NF. (c) An enlarged visualization of the heterostructures with Co_9S_8 nanoflakes surrounding Co_3O_4 and the corresponding FFT. Yellow represents Co_9S_8, blue represents Co_3O_4, and green represents the heterogeneous zone. (d) Reverse FFT filtered fringes of (311) plane of Co_9S_8 and (331) plane of Co_3O_4 in (c). (e) EDS element mapping images of Co, O and S elements of the sample Co_9S_8@Co_3O_4/NF.

The micro-nano structures of prepared materials were also characterized by TEM for more details. Compared to $Co(CO_3)_{0.5}(OH)_{0.11}\cdot H_2O$, the Co_3O_4 nanoneedle is composed of many nanoparticles with a size of 10–20 nm. Such a porous structure is formed due to the escaping CO_2 and H_2O (Fig. S4(a) in the ESM). The lattice spacing of 0.24 nm matches the (311) face of the Co_3O_4 spinel (Fig. S4(c) in the ESM). Meanwhile, the interplanar distance of 0.23 nm in Fig. S4(d) in the ESM corresponds to the lattice spacing of (331) for Co_9S_8. The Co_9S_8/Co_3O_4 hybrid with the porous hierarchical structure and rich heterointerfaces can be clearly observed (Fig. S5 in the ESM), which contributes to increasing the specific surface area of the catalysts and do the favor to the electrocatalytic process. As for the high-resolution TEM (HRTEM) of $Co_9S_8@Co_3O_4$/NF (Fig. 2(b)), the (331), (400) and (311) crystal planes of Co_9S_8 can be detected in the external nanoflakes while the inner lattice corresponds to the (331) face of Co_3O_4. This result confirms the hierarchical porous structure of the $Co_9S_8@Co_3O_4$/NF with the Co_3O_4 core encapsulated by Co_9S_8 nanoflakes. Zooming in the connection area of the two phases (Fig. 2(c)), there is no directly touched heterointerface but a heterogeneous zone with an irregular lattice arrangement. The crystal planes on two sides can be confirmed as (311) of Co_9S_8 and (331) of Co_3O_4 by fast Fourier transform (FFT), respectively. Noticeably, the corresponding inverse FFT diagram (Fig. 2(d)) indicates that the heterogeneous zone merges the orientation characteristics of the two crystal planes. The lattice spacing in the range of 0.22–0.35 nm is different from 0.18 nm (331) nor 0.30 nm (311), showing a distorted arrangement and reduced degree of order. The existence of this heterogeneous interface zone is precisely due to the epitaxial growth toward cobalt sulfide with cobalt oxide as the cobalt source, which impels sulfur doping into Co_3O_4 and oxygen into Co_9S_8. Energy dispersive spectra (EDS) element mapping of $Co_9S_8@Co_3O_4$/NF hybrid in Fig. 2(e) shows that the Co and S are uniformly distributed on the whole nanoarchitecture. In contrast, the O element concentrates inside the region, which further confirms the heterogeneous nanostructure with Co_9S_8 shell and Co_3O_4 core.

The surface elemental compositions and valence states of samples were analyzed by XPS (Fig. 3). The XPS survey spectrum of $Co_9S_8@Co_3O_4$/NF in Fig. 3(a) indicates the presence of Co, O, and S elements, confirming that the sulfur is successfully introduced into the surface. The XPS survey spectra of Co_3O_4/NF and Co_9S_8/NF are also shown in Fig. S6 in the ESM. For the high-resolution Co 2p XPS spectra of Co_3O_4/NF (Fig. 3(b)), the peaks of 796.2, 780.3 and 785.3 eV match well with previously reported Co_3O_4 [53–55]. As for $Co_9S_8@Co_3O_4$/NF, the peaks located at 796.8 and 781.1 eV correspond to Co $2p_{1/2}$ and Co $2p_{3/2}$, respectively, as well as a satellite peak at 786.1 eV. Furthermore, the peak of 775.6 eV can be assigned to the Co–S bond [56, 57], illustrating that the surface of Co_3O_4 has been converted to Co_9S_8. Compared with the peaks at 796.6, 780.9, 785.5 and 786.1 eV of Co_9S_8, the peaks of $Co_9S_8@Co_3O_4$/NF exhibit a positive shift about 0.1 eV, indicative of the strong electronic interactions between Co_3O_4 and Co_9S_8. As for S 2p spectra (Fig. 3(c)), the peaks at 162.1 and 163.8 eV of $Co_9S_8@Co_3O_4$ are assigned to S $2p_{3/2}$ and S $2p_{1/2}$, respectively [58]. Otherwise, the peak at 162.1 eV is attributed to the low surface coordination of S^{2-} and the peak at 163.8 eV comes from the metal–sulfur bond [59]. Meanwhile, a positive shift of about 0.2 eV of S $2p_{3/2}$ and S $2p_{1/2}$ in $Co_9S_8@Co_3O_4$/NF compared with that in Co_9S_8/NF (161.9 eV and 163.6 eV), suggests a changed electron density around S after introducing the sulfide. The high-resolution O 1s spectra of $Co_9S_8@Co_3O_4$/NF and Co_3O_4/NF are shown in Fig. 3(d). The two peaks of 531.2 and 532.4 eV in $Co_9S_8@Co_3O_4$/NF can be indexed to oxygen-containing groups on the surface [26, 60]. Compared to Co_3O_4/NF, these peaks are slightly shifted due to the generation of heterogeneous interface zones. Moreover, the peak of lattice oxygen at 529.6 eV disappears in the $Co_9S_8@Co_3O_4$, which affirms the formation of Co_9S_8 on the surface of Co_3O_4 nanoneedle heterostructures.

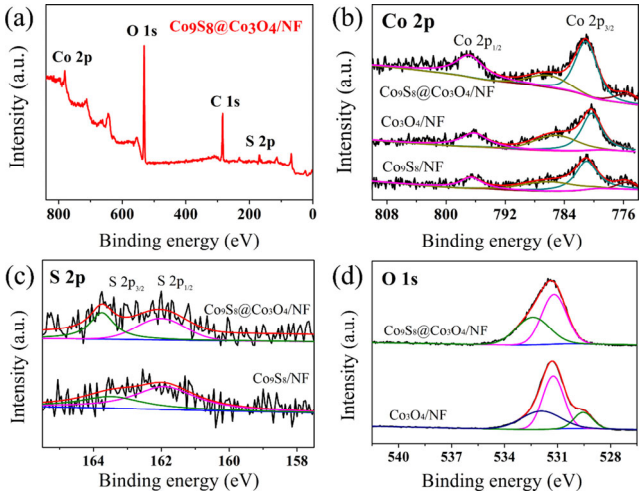

Figure 3 (a) XPS survey spectra of $Co_9S_8@Co_3O_4$/NF. (b)–(d) High-resolution spectra of Co 2p, S 2p, and O 1s of Co_3O_4/NF, $Co_9S_8@Co_3O_4$/NF, and Co_9S_8/NF, respectively.

In order to explore the effect of the special heterostructure, the catalytic performance of obtained samples toward HER and OER was evaluated. Bare Ni foam (NF) and commercial RuO_2 loading on Ni foam (RuO_2/NF) were also tested for comparison (Fig. S7 in the ESM). In Fig. 4(a), the $Co_9S_8@Co_3O_4$/NF only requires an overpotential of 331 mV to reach a large OER current density of 100 mA·cm^{-2}, which is significantly lower than those of bare Ni foam (706 mV), Co_9S_8/NF (444 mV) and Co_3O_4/NF (518 mV, Fig. S8(a) in the ESM). Combined with the

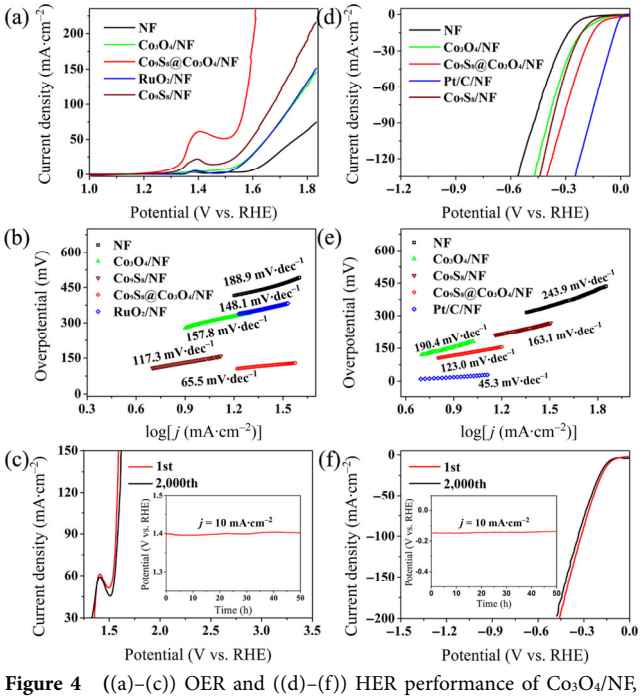

Figure 4 ((a)–(c)) OER and ((d)–(f)) HER performance of Co_3O_4/NF, $Co_9S_8@Co_3O_4$/NF, Co_9S_8/NF, bare NF, commercial Pt/C and RuO_2 in 1 M KOH. (a) and (d) Polarization curves of the samples at a scan rate of 5 mV·s^{-1}. (b) and (e) Corresponding Tafel plots. (c) and (f) Polarization curves of $Co_9S_8@Co_3O_4$/NF before and after 2,000 CV cycles for OER and HER, respectively. Insets of (c) and (f) show the chronopotentiometry curves of $Co_9S_8@Co_3O_4$/NF at a constant current density of 10 mA·cm^{-2}.

limited OER activity of $Co(CO_3)_{0.5}(OH)_{0.11}\cdot H_2O$/NF (Fig. S9(a) in the ESM), the superior performance of Co_9S_8@Co_3O_4/NF demonstrates that the heterogeneous zones between Co_9S_8 and Co_3O_4 play an essential role in reducing the OER overpotentials. Moreover, the presented OER performance of Co_9S_8@Co_3O_4/NF even far exceeds that of state-of-art RuO_2 (515 mV) and ranks as one of the most active nonprecious-metal-based electrocatalysts (Table S1 in the ESM).

Besides, the fitted Tafel value of Co_9S_8@Co_3O_4/NF catalyst is 65.5 mV·dec^{-1}, lower than those of Co_3O_4/NF (157.8 mV·dec^{-1}), Co_9S_8/NF (117.3 mV·dec^{-1}), RuO_2/NF (148.1 mV·dec^{-1}) and bare Ni foam (188.9 mV·dec^{-1}, Fig. 4(b)), illustrating more favorable OER kinetics. Additionally, the long-term stability was tested by cyclic voltammetry (CV) and chronopotentiometry methods. The LSV curve of Co_9S_8@Co_3O_4/NF catalyst almost maintains the same after 2,000 consecutive cycles (Fig. 4(c)), indicating an excellent OER durability. This is further corroborated by the chronopotentiometry curve with no noticeable degradation after 50 h at 10 mA·cm^{-2} (inset of Fig. 4(c)).

To develop the bifunctional activity for water splitting, the HER performances of all prepared samples and commercial Pt/C were evaluated (Fig. 4(d) in the ESM). The Co_9S_8@Co_3O_4/NF delivers the best performance with an overpotential of 130 mV at 10 mA·cm^{-2}, much lower than those of NF (263 mV), Co_3O_4/NF (177 mV) and Co_9S_8/NF (188 mV, Fig. S8(b) in the ESM) and also superior to the reported transition-metal-based nanocatalysts (Table S2 in the ESM). Moreover, the Tafel slope of Co_9S_8@Co_3O_4/NF for HER is determined to be 123.0 mV·dec^{-1} (Fig. 4(e)), much smaller than those of Co_3O_4/NF (190.4 mV·dec^{-1}), Co_9S_8/NF (163.1 mV·dec^{-1}) and NF (243.9 mV·dec^{-1}). It proves that the enhanced HER reaction kinetics belongs to the Volmer-Heyrovsky mechanism [34], benefiting from the Co_9S_8/Co_3O_4 coupled heterostructures. The HER stability testing shows that the polarization curve of Co_9S_8@Co_3O_4/NF maintains unchanged after 2,000 cycles (Fig. 4(f)). Besides, no apparent degradation can be detected on the HER overpotential of Co_9S_8@Co_3O_4/NF after continuous operation for 50 h (inset of Fig. 4(f)), suggesting the remarkable durability of the novel heterostructure nanocomposite. Therefore, considering the excellent OER and HER electrocatalytic properties, the designed Co_9S_8@Co_3O_4/NF heterogeneous electrode shows excellent potential for practical water splitting application.

The Co_9S_8@Co_3O_4/NF heterostructures with different S contents were also synthesized at different amounts of added Na_2S in the sulfidation step (Fig. S10 in the ESM). Electrochemical tests show that an appropriate S content in the Co_9S_8@Co_3O_4/NF hybrid achieves the best HER and OER performance while an excessive one hinders the catalytic behavior (Fig. S11 in the ESM). To essentially explore the reason for the enhanced bifunctional activity of Co_9S_8@Co_3O_4/NF, the reaction resistance was measured by EIS. As displayed in Figs. 5(a), 5(b) and Fig. S12 in the ESM, Co_9S_8@Co_3O_4/NF gives the lowest charge transfer resistance value (R_{ct}) compared with single-phase Co_3O_4/NF and Co_9S_8/NF as well as the $Co(CO_3)_{0.5}(OH)_{0.11}\cdot H_2O$/NF (Tables S3 and S4 in the ESM), indicating the highly efficient electron transfer during OER and HER processes. It is generally known that oxide performs poor conductivity in comparison to sulfide. Therefore, the enhanced efficient charge transfer of Co_9S_8@Co_3O_4/NF is attributed to the introduction of Co_9S_8 and the presence of the heterogeneous interface zone between Co_9S_8 and Co_3O_4. N_2 adsorption–desorption isotherms demonstrate that the BET specific surface areas are determined to be about 40.4, 17.7 and 18.1 m^2·g^{-1} for Co_9S_8@Co_3O_4/NF, Co_3O_4/NF and Co_9S_8/NF, respectively (Fig. 5(c) in the ESM). This is because that the formation of Co_9S_8 nanoflakes on Co_3O_4 nanoarrays could

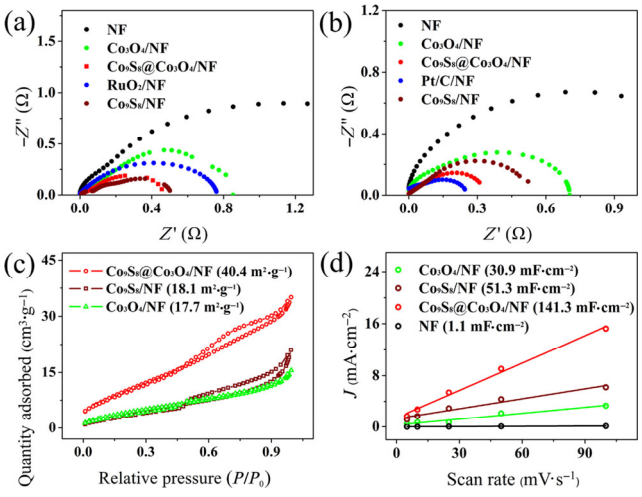

Figure 5 EIS Nyquist plots for (a) OER at 1.62 V vs. RHE and (b) HER at −0.43 V vs. RHE of Co_3O_4/NF, Co_9S_8/NF, Co_9S_8@Co_3O_4/NF, bare NF, Pt/C/NF and RuO_2/NF, respectively. Insets in (a) and (b) show simplified equivalent circuits. (c) N_2 adsorption–desorption isotherms and specific surface areas. (d) ECSA values are determined by the C_{dl} method.

expose more physical surface area. However, the excessive sulfuration leads to the growth of more extensive and thicker Co_9S_8 nanoflakes, which destroy the nanoarray structure and reduce the surface area. Hence, such a unique hierarchical porous structure could provide sufficient contact area with electrolyte, facilitating the mass transfer process. Furthermore, electrochemical surface area (ECSA) was determined by the electrical double-layer capacitance (C_{dl}). The corresponding C_{dl} values of Co_9S_8@Co_3O_4/NF, Co_3O_4/NF and Co_9S_8/NF are calculated to be 141.3, 30.9 and 51.3 mF·cm^{-2} (Fig. 6(d) and Fig. S13 in the ESM), respectively. The ECSA value (Fig. S14 in the ESM) of Co_9S_8@Co_3O_4/NF is about 4.5 times higher than that of Co_3O_4/NF, while the BET area is only 2.3 times, highlighting the critical role of heterostructure nanointerface zone in activating more electrochemical active sites for the catalytic reactions. Besides, the normalized density of Co_9S_8@Co_3O_4/NF is better than those of Co_3O_4/NF and Co_9S_8/NF (Table S5 in the ESM), identifying the increased intrinsic activity. These results demonstrate that the oxide/sulfide

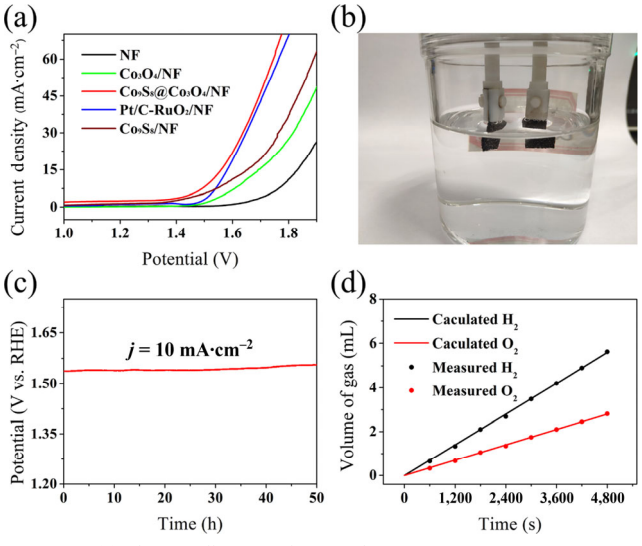

Figure 6 (a) The overall water-splitting polarization curves in 1.0 M KOH at 5 mV·s^{-1}. (b) The digital photograph of overall water-splitting using Co_9S_8@Co_3O_4/NF catalyst for cathode and anode at 10 mA·cm^{-2}. (c) Continuous overall water-splitting of Co_9S_8@Co_3O_4/NF at 10 mA·cm^{-2} for 50 h. (d) The theoretical and experimental gas volumes of H_2 and O_2 versus time.

heterogeneous hybrid can synergistically accelerate the charge transfer and increase active areas, resulting in superior HER and OER performance.

To further study the accessible potential for overall water-splitting, the synthesized catalyst was constructed as cathode and anode in a two-electrode electrolytic setup. Significantly, the Co_9S_8@Co_3O_4/NF heterostructure affords a potential of 1.52 V at 10 mA·cm^{-2} (Fig. 6(a) in the ESM), which is lower than those of single Co_3O_4/NF (1.64 V), Co_9S_8/NF (1.59 V), and $Co(CO_3)_{0.5}(OH)_{0.11}\cdot H_2O$/NF (1.70 V, Fig. S15 in the ESM), affirming the essential effect of the heterogeneous zone between oxide and sulfide. Such a high activity of Co_9S_8@Co_3O_4/NF hybrid even outperforms the commercial Pt/C-RuO_2/NF couple (1.56 V) and other previously related electrocatalysts for overall water-splitting (Table S6 in the ESM). In addition, as shown in Fig. 6(b) in the ESM, many gas bubbles can be clearly observed on both anode and cathode electrodes when the electrolyzer is working, demonstrating the high energy efficiency and potential application. More fortunately, Co_9S_8@Co_3O_4/NF heterogeneous arrays display superior durability with negligible performance reduction for more than 50 h continuous electrolysis at 10 mA·cm^{-2} (Fig. 6(c)). In addition, a good stability can be still maintained at a large current of 50 mA·cm^{-2} (Fig. S16 in the ESM). The remained hierarchical heterostructures of Co_9S_8@Co_3O_4/NF nanoarrays after the long-term operation further evidence its outstanding structural stability (Fig. S17 in the ESM). Further XPS and TEM results (Figs. S18 and S19 in the ESM) show that amorphous cobalt oxide and oxyhydroxide are formed on the surface after long-term test [61]. Meanwhile, the Faradaic efficiency (FE) of the Co_9S_8@Co_3O_4/NF electrochemical system is almost 100% for both OER and HER processes (Fig. 6(d) in the ESM), proving the excellent catalytic activity of the Co_9S_8@Co_3O_4/NF hybrid electrode. Refer to the above-enhanced properties, the construction of Co_9S_8@Co_3O_4/NF alkaline electrolyzer is of great significance for both academic and industrial areas.

To better understand the synergistic effect of heterointerface zone on overall water-splitting catalytic performance, we carried out DFT to calculate the chemisorption energies of hydrogen (ΔG_H) and hydroxide (ΔG_{OH}) for the surface of Co_3O_4, S-doped Co_3O_4, Co_9S_8, and O-doped Co_9S_8 surface (Fig. 7(a)). It should be noted that there is only one position for S-doped Co_3O_4 while there are six different sites for O-doped Co_9S_8 surface (Figs. S20 and S21 in the ESM). Based on the principle of minimizing energy, the most stable model was selected for the subsequent computations (Table S7 in the ESM). As we all know, the value of Gibbs free energy for H adsorption (ΔG_H) can be employed to evaluate the HER activity [62]. It is generally believed that when the ΔG_H value is close to 0, HER reaction is favorable to occur, which means a higher HER activity [63]. As shown in Fig. 7(b) in the ESM, for the surface of Co_3O_4, the calculated ΔG_H on Co site (Co_3O_4-Co-H) and O site (Co_3O_4-O-H) is as high as 0.58 and 0.65 eV, respectively, indicating that the HER performance of S-free Co_3O_4 surface is poor. Next, we constructed an element-doped model to simulate the heterointerfaces at the atomic level for the calculation. When S is doped into Co_3O_4 surface, the free energy of H on Co site (S/Co_3O_4-Co-H) is decreased to 0.43 eV, revealing that the incorporation of S can enhance the HER activity of Co_3O_4 matrix. It is worth noting that the ΔG_H value of S/Co_3O_4-S-H is almost close to 0 (0.01 eV), suggesting S atoms in Co_3O_4 of nanointerface actually act as the highly active sites for HER. As for the case of Co_9S_8, the ΔG_H on two kinds of S sites (i.e., S1 and S2) is 1.18 eV (Co_9S_8-S1-H) and 0.74 eV (Co_9S_8-S2-H), which is much larger than those on the

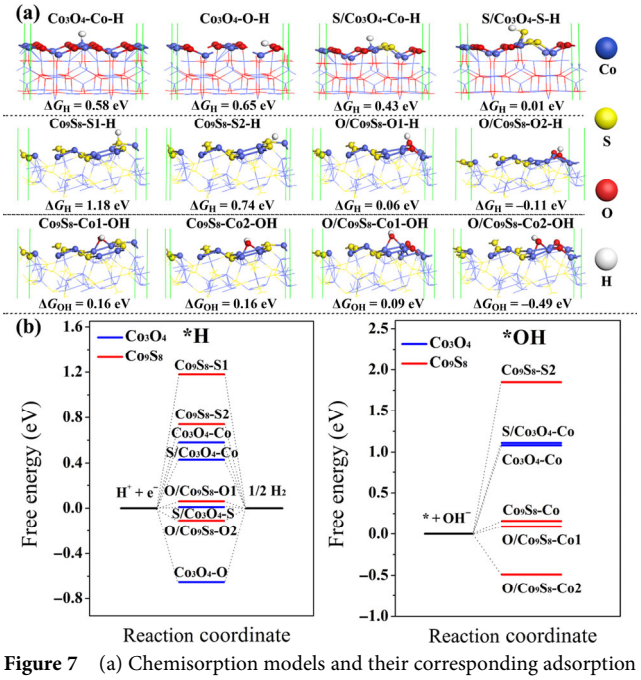

Figure 7 (a) Chemisorption models and their corresponding adsorption energies of H and OH intermediates on Co_9S_8, S-doped Co_3O_4 and O-doped Co_9S_8. (b) The free energy diagrams of H and OH on Co_3O_4, Co_9S_8, S-doped Co_3O_4 and O-doped Co_9S_8.

surface of O-doped Co_9S_8 (two kinds of O sites: O/Co_9S_8-O1-H (0.06 eV), O/Co_9S_8-O2-H (−0.11 eV)). These results reveal that both doped S into Co_3O_4 and doped O into Co_9S_8 could efficiently improve the HER performance of resultant hybrids. Thus, it is concluded that the Co_3O_4/Co_9S_8 heterostructure possesses much higher HER catalytic activity than those of individual Co_3O_4 and Co_9S_8, consistent with the experimental analysis. Moreover, to evaluate the OER process (Fig. 7(c)), the adsorption ability for OH^- on the interfacial sites was calculated. As expected, the adsorption free energy value for OH^- on two kinds of Co sites (i.e., Co1 and Co2) of O-doped Co_9S_8 (ΔG_{OH} = −0.49 eV and 0.09 eV) is much lower than that of O-free Co_9S_8 (ΔG_{OH} = 0.16 eV), which means that the OH^- group can be absorbed on the surface of O-doped Co_9S_8 more easily, and thus the OER performance can be significantly facilitated. In particular, activated by the doped negative O atoms, the Co2 site in O-doped Co_9S_8 shows the strongest adsorption for OH^-, suggesting that the Co2 site at the interface acts as a more efficient site for catalyzing OER. The high consistency between theoretical and experimental demonstrates that the synergistically promoted adsorption and cleavage of H_2O molecule on the heterogeneous interface is the reason for the enhanced hydrolysis performance on Co_9S_8@Co_3O_4/NF hybrid nanocatalysts. In summary, the excellent catalytic activity is attributed to the following advantages: (i) Highly conductive Ni support facilitates the efficient charge transfer; (ii) porous core shell nanoarchitecture benefits the infiltration and transportation of gas/ions; (iii) heterogeneous interface zone synergistically favors the chemisorption energy of hydrogen and oxygen intermediates.

4 Conclusions

To sum up, we have successfully synthesized a hierarchically porous hybrid heterostructure on Ni foam, which is consisted of Co_9S_8 nanoflakes supported on Co_3O_4 nanoneedles, via a simple, efficient, and low-temperature step-wise strategy. The novel core-shell Co_9S_8@Co_3O_4/NF nanoarrays with high specific surface area and enriched heterostructures exhibit excellent bifunctional catalytic activities and long-term stability in an

alkaline environment. The Co_9S_8@Co_3O_4/NF catalyst can be accessible for both HER and OER in overall water splitting, and the cell voltage to afford 10 mA·cm^{-2} is as low as 1.52 V, which even surpasses Pt/C-RuO_2 couple and previously developed earth-abundant electrocatalysts. The excellent catalytic performance of Co_9S_8@Co_3O_4/NF can be attributed to its good electrical conductivity, the porous core–shell nanoarchitecture and the interfacial effect between the two heterogeneous phases. Further analysis by DFT calculation reveals that the synergistic effect between Co_9S_8 and Co_3O_4 at the interface indeed increases active sites with high reactivity for water splitting, deepening the understanding of the Co_9S_8/Co_3O_4 heterogeneous interface zone synergistic mechanism. This work provides a controllable and efficient method for the growth of heterostructure nanocomposites, which can shed light on the rational design and interface engineering of high-performance hybrid nanomaterials for energy-related technologies.

Acknowledgements

This work was supported by the National Natural Science Foundation of China (51972224).

Electronic Supplementary Material: Supplementary material (additional material characterization such as SEM images, TEM images, XPS, XRD and OER performance of the contrast samples, tables on comparisons of electrochemical performances, simulation details) is available in the online version of this article at https://doi.org/10.1007/s12274-021-3632-4.

References

[1] Guo, Y. N.; Park, T.; Yi, J. W.; Henzie, J.; Kim, J.; Wang, Z. L.; Jiang, B.; Bando, Y.; Sugahara, Y.; Tang, J. et al. Nanoarchitectonics for transition-metal-sulfide-based electrocatalysts for water splitting. *Adv. Mater.* **2019**, *31*, e1807134.

[2] She, Y. Y.; Liu, J.; Wang, H. K.; Li, L.; Zhou, J. S.; Leung, M. K. H. Bubble-like Fe-encapsulated N, S-codoped carbon nanofibers as efficient bifunctional oxygen electrocatalysts for robust Zn–air batteries. *Nano Res.* **2020**, *13*, 2175–2182.

[3] Li, X.; Wang, J. One-dimensional and two-dimensional synergized nanostructures for high-performing energy storage and conversion. *InfoMat* **2020**, *2*, 3–32.

[4] Sun, J. P.; Hu, X. T.; Huang, Z. D.; Huang, T. X.; Wang, X. K.; Guo, H. L.; Dai, F. N.; Sun, D. F. Atomically thin defect-rich Ni–Se–S hybrid nanosheets as hydrogen evolution reaction electrocatalysts. *Nano Res.* **2020**, *13*, 2056–2062.

[5] Dong, B. B.; Cui, J. Y.; Liu, T. F.; Gao, Y. Y.; Qi, Y. Y.; Li, D.; Xiong, F. Q.; Zhang, F. X.; Li, C. Development of novel perovskite–like oxide photocatalyst $LiCuTa_3O_9$ with dual functions of water reduction and oxidation under visible light irradiation. *Adv. Energy Mater.* **2018**, *8*, 1801660.

[6] Ali, A.; Shen, P. K. Recent progress in graphene-based nanostructured electrocatalysts for overall water splitting. *Electrochem. Energ. Rev.* **2020**, *3*, 370–394.

[7] Zou, Z. X.; Wang, X. Y.; Huang, J. S.; Wu, Z. C.; Gao, F. An Fe-doped nickel selenide nanorod/nanosheet hierarchical array for efficient overall water splitting. *J. Mater. Chem. A* **2019**, *7*, 2233–2241.

[8] You, B.; Zhang, Y. D.; Yin, P. Q.; Jiang, D. E.; Sun, Y. J. Universal molecular-confined synthesis of interconnected porous metal oxides–N–C frameworks for electrocatalytic water splitting. *Nano Energy* **2018**, *48*, 600–606.

[9] Han, N. N.; Yang, K. R.; Lu, Z. Y.; Li, Y. J.; Xu, W. W.; Gao, T. F.; Cai, Z.; Zhang, Y.; Batista, V. S.; Liu, W. et al. Nitrogen–doped tungsten carbide nanoarray as an efficient bifunctional electrocatalyst for water splitting in acid. *Nat. Commun.* **2018**, *9*, 924.

[10] Wang, Z. Y.; Yang, J.; Wang, W. Y.; Zhou, F. Y.; Zhou, H.; Xue, Z. G.; Xiong, C.; Yu, Z. Q.; Wu, Y. Hollow cobalt–nickel phosphide nanocages for efficient electrochemical overall water splitting. *Sci. China Mater.* **2020**, *64*, 861–869.

[11] Menezes, P. W.; Indra, A.; Zaharieva, I.; Walter, C.; Loos, S.; Hoffmann, S.; Schlögl, R.; Dau, H.; Driess, M. Helical cobalt borophosphates to master durable overall water-splitting. *Energy Environ. Sci.* **2019**, *12*, 988–999.

[12] Zhou, H. Q.; Yu, F.; Zhu, Q.; Sun, J. Y.; Qin, F.; Yu, L.; Bao, J. M.; Yu, Y.; Chen, S.; Ren, Z. F. Water splitting by electrolysis at high current densities under 1.6 volts. *Energy Environ. Sci.* **2018**, *11*, 2858–2864.

[13] Du, C. F.; Sun, X. L.; Yu, H.; Fang, W.; Jing, Y.; Wang, Y. H.; Li, S. Q.; Liu, X. H.; Yan, Q. Y. $V_4C_3T_x$ MXene: A promising active substrate for reactive surface modification and the enhanced electrocatalytic oxygen evolution activity. *InfoMat* **2020**, *2*, 950–959.

[14] He, Y.; Zhang, J. F.; He, G. W.; Han, X. P.; Zheng, X. R.; Zhong, C.; Hu, W. B.; Deng, Y. D. Ultrathin Co_3O_4 nanofilm as an efficient bifunctional catalyst for oxygen evolution and reduction reaction in rechargeable zinc-air batteries. *Nanoscale* **2017**, *9*, 8623–8630.

[15] Han, X. P.; Wu, X. Y.; Deng, Y. D.; Liu, J.; Lu, J.; Zhong, C.; Hu, W. B. Ultrafine Pt nanoparticle-decorated pyrite-type CoS_2 nanosheet arrays coated on carbon cloth as a bifunctional electrode for overall water splitting. *Adv. Energy Mater.* **2018**, *8*, 1800935.

[16] Zheng, X. R.; Wu, X. Y.; Han, X. P.; Deng, Y. D.; Wang, J. H. *In-situ* multi-deposition process for cobalt–sulfide synthesis with efficient bifunctional catalytic activity. *Ferroelectrics* **2018**, *523*, 119–125.

[17] Chen, Z. J.; Duan, X. G.; Wei, W.; Wang, S. B.; Zhang, Z. J.; Ni, B. J. Boride-based electrocatalysts: Emerging candidates for water splitting. *Nano Res.* **2020**, *13*, 293–314.

[18] Zhou, Y. F.; Wang, Z. X.; Pan, Z. Y.; Liu, L.; Xi, J. Y.; Luo, X. L.; Shen, Y. Exceptional performance of hierarchical Ni–Fe (hydr)oxide@NiCu electrocatalysts for water splitting. *Adv. Mater.* **2019**, *31*, 1806769.

[19] Zhao, C. Y.; Zhang, Y. F.; Chen, L. F.; Yan, C. Y.; Zhang, P. X.; Ang, J. M.; Lu, X. H. Self-assembly-assisted facile synthesis of MoS_2-based hybrid tubular nanostructures for efficient bifunctional electrocatalysis. *ACS Appl. Mater. Inter.* **2018**, *10*, 23731–23739.

[20] Zang, X. N.; Chen, W. S.; Zou, X. L.; Hohman, J. N.; Yang, L. J.; Li, B. X.; Wei, M. S.; Zhu, C. H.; Liang, J. M.; Sanghadasa, M. et al. Self–assembly of large-area 2D polycrystalline transition metal carbides for hydrogen electrocatalysis. *Adv. Mater.* **2018**, *30*, 1805188.

[21] Huang, G.; Xiao, Z. H.; Chen, R.; Wang, S. Y. Defect engineering of cobalt-based materials for electrocatalytic water splitting. *ACS Sustain. Chem. Eng.* **2018**, *6*, 15954–15969.

[22] Zhou, Q. Q.; Li, T. T.; Qian, J. J.; Hu, Y.; Guo, F. Y.; Zheng, Y. Q. Self–supported hierarchical CuO_x@Co_3O_4 heterostructures as efficient bifunctional electrocatalysts for water splitting. *J. Mater. Chem. A* **2018**, *6*, 14431–14439.

[23] Liu, X. J.; Xi, W.; Li, C.; Li, X. B.; Shi, J.; Shen, Y. L.; He, J.; Zhang, L. H.; Xie, L.; Sun, X. M. et al. Nanoporous Zn-doped Co_3O_4 sheets with single-unit-cell-wide lateral surfaces for efficient oxygen evolution and water splitting. *Nano Energy* **2018**, *44*, 371–377.

[24] Li, C. C.; Hou, J. X.; Wu, Z. X.; Guo, K.; Wang, D. L.; Zhai, T. Y.; Li, H. Q. Acid promoted Ni/NiO monolithic electrode for overall water splitting in alkaline medium. *Sci. China Mater.* **2017**, *60*, 918–928.

[25] Zu, D.; Wang, H. Y.; Lin, S.; Ou, G.; Wei, H. H.; Sun, S. Q.; Wu, H. Oxygen-deficient metal oxides: Synthesis routes and applications in energy and environment. *Nano Res.* **2019**, *12*, 2150–2163.

[26] Wu, M. J.; Zhang, G. X.; Tong, H.; Liu, X. H.; Du, L.; Chen, N.; Wang, J.; Sun, T. X.; Regier, T.; Sun, S. H. Cobalt (II) oxide nanosheets with rich oxygen vacancies as highly efficient bifunctional catalysts for ultra–stable rechargeable Zn–air flow battery. *Nano Energy* **2021**, *79*, 105409.

[27] Li, C.; Han, X. P.; Cheng, F. Y.; Hu, Y. X.; Chen, C. C.; Chen, J. Phase and composition controllable synthesis of cobalt manganese spinel nanoparticles towards efficient oxygen electrocatalysis. *Nat. Commun.* **2015**, *6*, 7345.

[28] Han, X. P.; He, G. W.; He, Y.; Zhang, J. F.; Zheng, X. R.; Li, L. L.; Zhong, C.; Hu, W. B.; Deng, Y. D.; Ma, T. Y. Engineering catalytic active sites on cobalt oxide surface for enhanced oxygen electrocatalysis. *Adv. Energy Mater.* **2018**, *8*, 1702222.

[29] Wu, H. M.; Feng, C. Q.; Zhang, L.; Zhang, J. J.; Wilkinson, D. P. Non–noble metal electrocatalysts for the hydrogen evolution reaction in water electrolysis. *Electrochem. Energ. Rev.* **2021**, doi: 10.1007/s41918-020-00086-z.

[30] Cabán-Acevedo, M.; Stone, M. L.; Schmidt, J. R.; Thomas, J. G.; Ding, Q.; Chang, H. C.; Tsai, M. L.; He, H. Jr.; Jin, S. Efficient hydrogen evolution catalysis using ternary pyrite–type cobalt phosphosulphide. *Nat. Mater.* **2015**, *14*, 1245–1251.

[31] Faber, M. S.; Dziedzic, R.; Lukowski, M. A.; Kaiser, N. S.; Ding, Q.; Jin, S. High-performance electrocatalysis using metallic cobalt pyrite (CoS_2) micro- and nanostructures. *J. Am. Chem. Soc.* **2014**, *136*, 10053–10061.

[32] Zhang, S. L.; Zhai, D.; Sun, T. T.; Han, A. J.; Zhai, Y. L.; Cheong, W. C.; Liu, Y.; Su, C. L.; Wang, D. S.; Li, Y. D. *In situ* embedding Co_9S_8 into nitrogen and sulfur codoped hollow porous carbon as a bifunctional electrocatalyst for oxygen reduction and hydrogen evolution reactions. *Appl. Catal., B–Environ.* **2019**, *254*, 186–193.

[33] Chen, Y. N.; Xu, S. M.; Zhu, S. Z.; Jacob, R. J.; Pastel, G.; Wang, Y. B.; Li, Y. J.; Dai, J. Q.; Chen, F. J.; Xie, H. et al. Millisecond synthesis of CoS nanoparticles for highly efficient overall water splitting. *Nano Res.* **2019**, *12*, 2259–2267.

[34] Li, J. W.; Xu, P. M.; Zhou, R. F.; Li, R.; Qiu, L. J.; Jiang, S. P.; Yuan, D. S. Co_9S_8–Ni_3S_2 heterointerfaced nanotubes on Ni foam as highly efficient and flexible bifunctional electrodes for water splitting. *Electrochim. Acta* **2019**, *299*, 152–162.

[35] Li, Y. X.; Yin, J.; An, L.; Lu, M.; Sun, K.; Zhao, Y. Q.; Gao, D. Q.; Cheng, F. Y.; Xi, P. X. FeS_2/CoS_2 interface nanosheets as efficient bifunctional electrocatalyst for overall water splitting. *Small* **2018**, *14*, 1801070.

[36] Xiong, Y.; Xu, L. L.; Jin, C. D.; Sun, Q. F. Interface-engineered atomically thin Ni_3S_2/MnO_2 heterogeneous nanoarrays for efficient overall water splitting in alkaline media. *Appl. Catal. B–Environ.* **2019**, *254*, 329–338.

[37] Liu, Y. K.; Jiang, S.; Li, S. J.; Zhou, L.; Li, Z. H.; Li, J. M.; Shao, M. F. Interface engineering of (Ni, Fe) S_2@MoS_2 heterostructures for synergetic electrochemical water splitting. *Appl. Catal. B–Environ.* **2019**, *247*, 107–114.

[38] Zhang, J.; Chen, Z. L.; Liu, C.; Zhao, J.; Liu, S. L.; Rao, D. W.; Nie, A.; Chen, Y. N.; Deng, Y. D.; Hu, W. B. Hierarchical iridium-based multimetallic alloy with double-core-shell architecture for efficient overall water splitting. *Sci. China Mater.* **2020**, *63*, 249–257.

[39] Yin, Y. J.; Tan, Y.; Wei, Q. Y.; Zhang, S. C.; Wu, S. Q.; Huang, Q.; Hu, F. L.; Mi, Y. Nanovilli electrode boosts hydrogen evolution: A surface with superaerophobicity and superhydrophilicity. *Nano Res.* **2021**, *14*, 961–968.

[40] Wu, X. Y.; Han, X. P.; Ma, X. Y.; Zhang, W.; Deng, Y. D.; Zhong, C.; Hu, W. B. Morphology-controllable synthesis of Zn-Co-mixed sulfide nanostructures on carbon fiber paper toward efficient rechargeable zinc-air batteries and water electrolysis. *ACS Appl. Mater. Inter.* **2017**, *9*, 12574–12583.

[41] Han, X. P.; Zhang, W.; Ma, X. Y.; Zhong, C.; Zhao, N. Q.; Hu, W. B.; Deng, Y. D. Identifying the activation of bimetallic sites in $NiCo_2S_4$@g–C_3N_4–CNT hybrid electrocatalysts for synergistic oxygen reduction and evolution. *Adv. Mater.* **2019**, *31*, 1808281.

[42] Liu, T. Y.; Diao, P. Nickel foam supported Cr-doped $NiCo_2O_4$/FeOOH nanoneedle arrays as a high-performance bifunctional electrocatalyst for overall water splitting. *Nano Res.* **2020**, *13*, 3299–3309.

[43] Clark, S. J.; Segall, M. D.; Pickard, C. J.; Hasnip, P. J.; Probert, M. I. J.; Refson, K.; Payne, M. C. First principles methods using CASTEP. *Z. Kristall.* **2005**, *220*, 567–570.

[44] Vanderbilt, D. Soft self–consistent pseudopotentials in a generalized eigenvalue formalism. *Phys. Rev. B* **1990**, *41*, 7892–7895.

[45] Perdew, J. P.; Burke, K.; Ernzerhof, M. Generalized gradient approximation made simple. *Phys. Rev. Lett.* **1996,** *77*, 3865.

[46] Nørskov, J. K.; Rossmeisl, J.; Logadottir, A.; Lindqvist, L.; Kitchin, J. R.; Bligaard, T.; Jónsson, H. Origin of the overpotential for oxygen reduction at a fuel–cell cathode. *J. Phys. Chem. B* **2004**, *108*, 17886–17892.

[47] Rossmeisl, J.; Nørskov, J. K.; Taylor, C. D.; Janik, M. J.; Neurock, M. Calculated phase diagrams for the electrochemical oxidation and reduction of water over Pt(111). *J. Phys. Chem. B* **2006**, *110*, 21833–21839.

[48] Stamenkovic, V.; Mun, B. S.; Mayrhofer, K. J. J.; Ross, P. N.; Markovic, N. M.; Rossmeisl, J.; Greeley, J.; Nørskov, J. K. Changing the activity of electrocatalysts for oxygen reduction by tuning the surface electronic structure. *Angew. Chem. Int., Ed.* **2006**, *45*, 2897–2901.

[49] Liu, S.; Cheng, H.; Xu, K.; Ding, H.; Zhou, J. Y.; Liu, B. J.; Chu, W. S.; Wu, C. Z.; Xie, Y. Dual modulation via electrochemical reduction activiation on electrocatalysts for enhanced oxygen evolution reaction. *ACS Energy Lett.* **2019**, *4*, 423–429.

[50] Scott, J. A.; Angeloski, A.; Aharonovich, I.; Lobo, C. J.; McDonagh, A.; Toth, M. *In situ* study of the precursor conversion reactions during solventless synthesis of Co_9S_8, Ni_3S_2, Co and Ni nanowires. *Nanoscale* **2018**, *10*, 15669–15676.

[51] Xie, B. Q.; Yu, M. Y.; Lu, L. H.; Feng, H. Z.; Yang, Y.; Chen, Y.; Cui, H. D.; Xiao, R. B.; Liu, J. Pseudocapacitive Co_9S_8/graphene electrode for high-rate hybrid supercapacitors. *Carbon* **2019**, *141*, 134–142.

[52] Yao, T. H.; Li, Y. L.; Liu, D. Q.; Gu, Y. P.; Qin, S. C.; Guo, X.; Guo, H.; Ding, Y. Q.; Liu, Q. M.; Chen, Q. et al. High-performance free–standing capacitor electrodes of multilayered Co_9S_8 plates wrapped by carbonized poly(3, 4-ethylenedioxythiophene): poly(styrene sulfonate)/reduced graphene oxide. *J. Power Sources* **2018**, *379*, 167–173.

[53] Feng, C.; Zhang, J. F.; He, Y.; Zhong, C.; Hu, W. B.; Liu, L.; Deng, Y. D. Sub-3 nm Co_3O_4 nanofilms with enhanced supercapacitor properties. *ACS Nano* **2015**, *9*, 1730–1739.

[54] Zhang, X.; Zhao, Y. Q.; Xu, C. L. Surfactant dependent self-organization of Co_3O_4 nanowires on Ni foam for high performance supercapacitors: from nanowire microspheres to nanowire paddy fields. *Nanoscale* **2014**, *6*, 3638–3646.

[55] Yu, Y. Y.; Zhang, J. L.; Zhong, M.; Guo, S. W. Co_3O_4 nanosheet arrays on Ni foam as electrocatalyst for oxygen evolution reaction. *Electrocatalysis* **2018**, *9*, 653–661.

[56] Zhang, Z. M.; Wang, Q.; Zhao, C. J.; Min, S. D.; Qian, X. Z. One–step hydrothermal synthesis of 3D petal-like Co_9S_8/RGO/Ni_3S_2 composite on nickel foam for high-performance supercapacitors. *ACS Appl. Mater. Inter.* **2015**, *7*, 4861–4868.

[57] Pu, J.; Wang, Z. H.; Wu, K. L.; Yu, N.; Sheng, E. H. Co_9S_8 nanotube arrays supported on nickel foam for high-performance supercapacitors. *Phys. Chem. Chem. Phys.* **2014**, *16*, 785–791.

[58] Gao, W. K.; Qin, J. F.; Wang, K.; Yan, K. L.; Liu, Z. Z.; Lin, J. H.; Chai, Y. M.; Liu, C. G.; Dong, B. Facile synthesis of Fe-doped Co_9S_8 nano-microspheres grown on nickel foam for efficient oxygen evolution reaction. *Appl. Surf. Sci.* **2018**, *454*, 46–53.

[59] Lv, Q. L.; Yang, L.; Wang, W.; Lu, S. Q.; Wang, T. E.; Cao, L. X.; Dong, B. H. One-step construction of core/shell nanoarrays with a holey shell and exposed interfaces for overall water splitting. *J. Mater. Chem. A* **2019**, *7*, 1196–1205.

[60] Weidler, N.; Schuch, J.; Knaus, F.; Stenner, P.; Hoch, S.; Maljusch, A.; Schäfer, R.; Kaiser, B.; Jaegermann, W. X-ray photoelectron spectroscopic investigation of plasma–enhanced chemical vapor deposited NiO_x, $NiO_x(OH)_y$, and $CoNiO_x(OH)_y$: influence of the chemical composition on the catalytic activity for the oxygen evolution reaction. *J. Phys. Chem. C* **2017**, *121*, 6455–6463.

[61] Huang, Z. F.; Wang, J.; Peng, Y. C.; Jung, C. Y.; Fisher, A.; Wang, X. Design of efficient bifunctional oxygen reduction/evolution electrocatalyst: recent advances and perspectives. *Adv. Energy Mater.* **2017**, *7*, 1700544.

[62] Wang, J.; Zhang, H.; Wang, X. Recent methods for the synthesis of noble-metal-free hydrogen-evolution electrocatalysts: From nanoscale to sub-nanoscale. *Small Methods* **2017**, *6*, 1700118.

[63] Du, F.; Shi, L.; Zhang, Y. T.; Li, T.; Wang, J. L.; Wen, G. H.; Alsaedi, A.; Hayat, T.; Zhou, Y.; Zou, Z. G. Foam–like Co_9S_8/Ni_3S_2 heterostructure nanowire arrays for efficient bifunctional overall water–splitting. *Appl. Catal., B–Environ.* **2019**, *253*, 246–252.